

Nano-size Joule-Heating to Achieve Low-Ohmic Ag–Si Contact on Boron Emitters of n-TOPCon Solar Cells

Rui Zhou, Yongsheng Li, Zhikun Zhang, Wenchang Tan,* Ziwei Chen,* Yuan Lin,* and Feng Pan*

Over the past decade, Tunnel Oxide Passivated Contact (TOPCon) solar cells have emerged as a leading technology for high-efficiency silicon solar cells. Conventional metallization processes using silver/aluminum (Ag/Al) pastes encounter significant hurdles due to reliability risks and insufficient contact quality. Recent advancements in laser-induced metallization technologies, particularly laser-enhanced contact optimization (LECO), offer promising solutions. However, the mechanism of silver-silicon (Ag–Si) contact formation on the P⁺ emitter of TOPCon cells via LECO processing remains incompletely understood. This study designs and prepares two types of glass frits (GF-A and GF-B) for TOPCon cells and investigates the electrical properties of corresponding devices. Advanced techniques are employed to examine the Ag–Si interfaces. The results demonstrate that GF-A-based TOPCon cells (Cell-A) outperformed GF-B-based cells (Cell-B) due to the construction of a current-confined Ag–Si interface. A composite conductive model for the Ag–Si interfaces by LECO treatment is introduced, revealing the nano-size Joule-heating to achieve the Ag–Si eutectic structure as the underlying formation mechanism. This work contributes to the understanding of metal-silicon contact optimization in solar cells and introduces novel methodologies for laser-induced synthesis and micro-nano interface engineering.

1. Introduction

Over the past decade, Tunnel Oxide Passivated Contact (TOPCon) solar cells have revolutionized the photovoltaic industry, emerging as a leading technology for high-efficiency silicon (Si) solar cells. As TOPCon technology evolves and becomes increasingly cost-effective, its advantages—such as exceptional conversion efficiency, minimal attenuation, and low temperature sensitivity—make it a compelling choice for mainstream solar applications.^[1] Despite these benefits, a critical challenge persists: achieving effective ohmic contact between the silver (Ag) electrodes and the low-doped P⁺ emitters.^[2]

In the conventional metallization process for TOPCon solar cells, silver/aluminum (Ag/Al) pastes are employed to form ohmic contacts on P⁺ emitters.^[3] However, this method relying on rapid sintering encounters significant hurdles. At temperatures exceeding the eutectic point of aluminum–silicon (Al–Si), aluminum diffuses into silicon, creating a P⁺⁺ emitter with reduced contact resistance but also

generating metallic spikes at the metal-silicon interface. This diffusion not only complicates the precise control of aluminum concentration and spike depth but also introduces metal recombination, leading to a decrease in photoelectric conversion efficiency (PCE).^[4] Moreover, the chemical interactions involving aluminum (especially the reaction with acetic acid) pose challenges to the stability of devices, necessitating costly encapsulation materials to prevent degradation.^[5]

Recent advancements in laser-induced metallization technologies offer promising solutions to these challenges. Laser-enhanced contact-optimization (LECO) technology represents a cutting-edge approach, originally developed to enhance the performance of passivated emitter and rear cells (PERC). By applying a reverse bias voltage and scanning a laser across the cell, LECO treatment facilitates the non-destructive injection of carriers, optimizing silver-silicon (Ag–Si) contacts precisely at the sites where the carrier short-circuit pathways are established.^[6] This technique has demonstrated significant improvements in PCE for PERC cells and holds the potential to address the issues faced by TOPCon cells. As evidenced by Krassowski et al., the implementation of a LECO-specialized Ag paste coupled with LECO

R. Zhou, Y. Li, W. Tan, F. Pan
School of Advanced Materials
Shenzhen Graduate School
Peking University
Shenzhen 518055, China
E-mail: tanwch@pku.edu.cn; panfeng@pku.edu.cn

Z. Zhang
Institute of Reactor Engineering Technology
China Institute of Atomic Energy
Beijing 102413, China

Z. Chen
Institute of Zhejiang University-Quzhou
Quzhou 324000, China
E-mail: chenzw@pku.edu.cn

Y. Lin
Key Laboratory of Photochemistry
Institute of Chemistry
Chinese Academy of Sciences
Beijing 100190, China
E-mail: linyuan@iccas.ac.cn

The ORCID identification number(s) for the author(s) of this article can be found under <https://doi.org/10.1002/sml.202409628>

DOI: 10.1002/sml.202409628

treatment led to a notable 0.38% increase in *PCE* of p-PERC solar cells, primarily due to enhancements in fill factor (*FF*) and open-circuit voltage (V_{oc}).^[7]

To delve deeper into the mechanisms underlying the enhancement, Großer et al.^[8] utilized the focused ion beam (FIB) technology, along with scanning electron microscopy and transmission electron microscopy (TEM), to uncover the buried Ag–Si interface and micro contacts on Phosphorus doped N^+ emitters induced by LECO treatment for p-PERC cells. And radially distributed Ag thread crystals were found to appear in the Si pyramids, forming Ag–Si alloy regions with a depth of ≈ 300 nm. Furthermore, Höffler et al.^[9] constructed a diode network model for p-PERC cells to simulate the current paths and current density in the LECO process and established the relationship between local thermal insulation and LECO activity at the Ag–Si interfaces.

Regarding TOPCon cells, Wu et al.^[10] validated that through the application of LECO treatment, the metallization of the P^+ emitter on TOPCon solar cells can be achieved using Al-free pastes, significantly enhancing the reliability of TOPCon solar cells. Fan et al.^[11] further investigated the Ag–Si interfaces of commercially produced TOPCon cells after LECO treatment, and revealed the presence of isotropic Ag–Si interdiffusion regions located proximate to the apex of the Si pyramids. This observation significantly contrasted with the Ag–Si interface typically observed in p-PERC cells. Nevertheless, the structure of Ag–Si interfaces remains devoid of a distinct physical depiction. In addition, given the inherent structural disparities between p-PERC and TOPCon cells, the current flow directions within the target emitters during the LECO process are different (from front Ag fingers to N^+ emitters in PERC cells and from P^+ emitters to front Ag fingers in TOPCon cells). Consequently, a comprehensive understanding of the formation mechanisms of Ag–Si contacts on P^+ emitters for TOPCon cells through LECO treatment remains elusive.

To address these research gaps, we designed and prepared two types of glass frits, respectively as glass frit A (GF-A) and glass frit B (GF-B). GF-A comprised a blend of oxides, including lead oxide (PbO), silicon dioxide (SiO_2), boron oxide (B_2O_3), and aluminum oxide (Al_2O_3), and endowed with a higher glass transition temperature (T_g) along with a lower flow and spreading ability. In contrast, GF-B was a traditional type of glass frit used in the front-side Ag paste, incorporating tellurium dioxide (TeO_2) as an additive to lower the T_g and improve the flow and spreading at the Ag–Si interfaces.^[12] The TOPCon cells Cell-A and Cell-B based on GF-A and GF-B respectively exhibited notable disparities in electrical properties after LECO treatment, with Cell-A significantly outperforming the other. Moreover, we conducted an exhaustive investigation of the Ag–Si interfaces by employing advanced techniques such as scanning electron microscope (SEM), Atomic Force Microscope (AFM), Kelvin probe force microscope (KPFM), and high-resolution transmission electron microscopy (HRTEM). And we demonstrated that Cell-A exhibited excellent suitability for creating laser-induced low-ohmic contacts due to the establishment of a current confined Ag–Si interface after rapid co-sintering. Furthermore, we introduced a composite conductive model for the enhanced Ag–Si interfaces by LECO treatment, which diverged significantly from the interfaces by conventional sintering pro-

cesses. The underlying formation mechanism was identified as the Ag–Si eutectic reaction via nano-size Joule heating. This work not only advanced the understanding of metal-silicon contact optimization in solar cells but also introduced novel methodologies for laser-induced synthesis and micro-nano interface engineering.

2. Results and Discussion

The preparation of Topcon solar cells primarily involves the following steps. First, Ag pastes were mixed by Ag powders and glass frits with organic vehicle and screen printed onto the Si wafers. Following this, the printed pastes undergo rapid sintering and then cooling to form Ag electrodes. Subsequently, LECO treatment was applied to form high-quality Ag–Si contacts. As shown in the schematic of LECO treatment in **Figure 1a**, a reverse bias voltage was used on the both sides of the cells and a laser scan was applied perpendicular to the Ag electrodes. **Figure S1** (Supporting Information) depicts the experimental setup for LECO treatment. This setup integrated a digital source meter, an electrode connection platform, and a laser system, enabling compatibility with diverse electrode patterns and scanning modalities. A schematic diagram of the TOPCon solar cells consists of a structure containing several key layers is also shown in **Figure 1a**. The TOPCon cells feature a traditional N-type cell design on the front side, with contacts formed by Ag fingers and P^+ emitters. On the back of the cells, an ultra-thin layer of silicon oxide (SiO_x) is first prepared, followed by the deposition of a thin layer of phosphorus-doped polycrystalline silicon (poly-Si) as the N^+ emitters.^[13] The combined ultra-thin SiO_x layer and poly-Si layer constitute an efficient passivated contact structure, significantly diminishing both surface and metal contact recombination. The Si wafers used in this work (53 mm \times 35 mm) were prepared through 182 mm \times 182 mm commercial TOPCon Si wafers through laser cutting. And **Figure S2a** (Supporting Information) displays the specific electrode pattern. The TOPCon solar cells in this work used the same electrode pattern on both the front and back sides to ensure symmetrical distribution of the electric field. Due to factors such as cutting damage and size reduction, the electrical performance of the devices in this work exhibited a discrepancy when compared to industrial data, but this did not compromise the discussion of the underlying mechanism. **Figure 1b** illustrates the variations in the current density–Voltage (J – V) curves of the sintered Cell-A and Cell-B before and subsequent undergoing LECO treatment. **Table S1** (Supporting Information) displays the specific electrical parameters of Cell-A and Cell-B, and the electrical parameters of the solar cell prepared by using Ag/Al paste (Cell-Ref) through traditional sintering process are also shown for reference. Before the LECO treatment, both the Cell-A and Cell-B exhibited exceedingly low short circuit current densities (J_{sc}), coupled with significantly diminished *FF*. These electrical parameters are far worse than Cell-Ref. This might be due to the absence of established efficient ohmic contacts at the Ag–Si interfaces on the P^+ emitters of the cells. And in comparison, the J_{sc} and *FF* of Cell-B are slightly higher than those of Cell-A. However, following the LECO treatment, the J_{sc} , *FF* and V_{oc} of both Cell-A and Cell-B showed significant improvement, with Cell-A exhibiting superior performance. This suggested that the LECO treatment effectively established

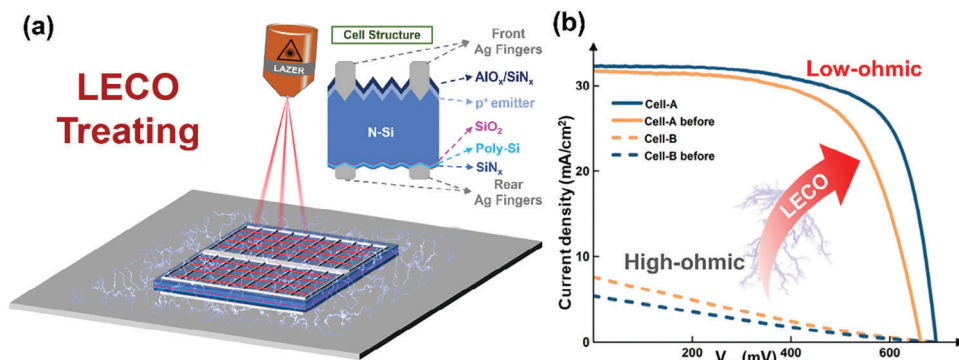


Figure 1. a) The manufacturing process of Topco solar cells prepared by LECO treatment and a typical structure of Topco solar cells; b) The J–V curves of Cell-A and Cell-B before and after LECO treatment. The dash lines indicate the J–V curves before LECO treatment and the solid lines indicate the curves after treatment.

optimized low-resistance contacts at the Ag–Si interfaces of the solar cells, and Cell-A benefit from better contact quality.

To further demonstrate that the difference in electrical performance between Cell-A and Cell-B was due to the interface quality enhanced by LECO treatment, AFM and KPFM testing were employed to characterize the Ag–Si contacts. The morphology characterized by AFM testing of the Ag–Si interface in Cell-A is displayed in Figure 2a₁, and the contact potential difference (CPD) measured by KPFM is shown in Figure 2a₂. By contrast, the morphology and CPD of the Ag–Si interface in Cell-B are respectively presented in Figure 2b₁,b₂. The dashed lines drawn in Figure 2a₁,b₁ are used to delineate the contours of the Si pyramids. It should be noted that the heights of the pyramids on the interfaces were not exactly uniform, since the cross-section samples were prepared using triple ion beam (FIB) cutting technology, and the locations on the cell surface bombarded with Ar⁺

were randomly selected. The morphology images reveal that the cross-section samples exhibited a smooth surface following Ar⁺ bombardment, with only a few voids remaining in the Ag fingers after sintering. From Figure 2a₂, a distinct boundary appeared beneath the pyramids, indicating a notable change in CPD in the area of Cell-A. On the contrary, Figure 2b₂ shows a blurred boundary along the edge of the pyramid in Cell B. To illustrate the changes more intuitively and quantitatively, the line distribution of CPD on the interface are collected and presented in Figure 2a₃,b₃ respectively for Cell-A and Cell-B. The specific collection positions are indicated by solid lines passing through the top of the pyramids in Figure 2a₁,b₁. As illustrated in Figure 2a₃, the change in CPD from the top of the pyramid to a depth of 2 μm into Si is 264.2 mV. In contrast, Figure 2b₃ shows a change of 91.4 mV over the same depth. This indicates that the Ag–Si of Cell-A interface exhibited superior charge transfer properties

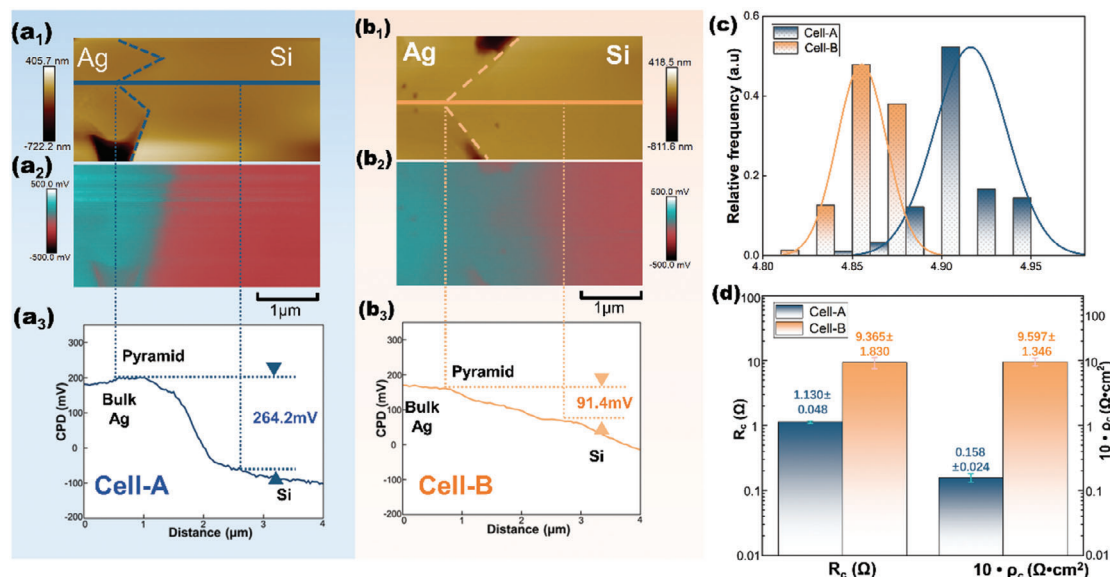


Figure 2. The results of AFM, KPFM, and the TLM measurement of the cells after LECO treatment. a₁) Morphology measured by AFM of the cross-section of Cell-A. a₂) The CPD measured by KPFM and a₃) the CPD line profile of Cell-A. b₁–b₃) Morphology image, CPD topographic maps, and the line profile for Cell-B. c) The frequency distribution of work function at the edges of pyramids on the Ag–Si interfaces of the cells. d) The R_c and ρ_c of the Cell-A and Cell-B.

and enhanced contact quality compared to Cell-B.^[14] In addition, we randomly collected the CPD values at the edge of the pyramid and converted them into corresponding work functions, and the frequency distribution of work function was shown in Figure 2c. The collected locations are shown in Figure S3a,b (Supporting Information).

To calibrate the work function of the probe, a standard material as gold (Au) was used with a known work function of 5.1 eV. The morphology image and CPD topographic map of Au are presented in Figure S4a,b (Supporting Information), respectively. As shown in Figure 2c, the frequency distribution center of Cell-A is 4.92 eV, while that of Cell-B is 4.85 eV. This indicates that at the edge of the pyramid, Cell-A was doped with a higher proportion of impurities than Cell-B and then the work function of the emitter was improved to a greater extent. The transfer length method (TLM) measurement was employed to measure the contact resistance (R_c) and the specific contact resistance (ρ_c) of the Cell-A and Cell-B, with the calculated results presented in Figure 2d. As shown in Figure 2d, Cell-A formed a Ag–Si interface with a significantly lower R_c of 1.130 Ω and ρ_c of 0.0158 $\Omega\cdot\text{cm}^2$, compared to Cell-B which exhibited an R_c of 9.365 Ω and ρ_c of 0.9597 $\Omega\cdot\text{cm}^2$ of Cell-B. Combining the results of AFM, KPFM and TLM testing, it was indicated that Cell-A achieved superior quality Ag–Si contact compared to Cell-B.

To further analyze the structural and compositional differences at the Ag–Si interfaces between Cell-A and Cell-B, TEM and energy dispersive spectrometer (EDS) measurements were conducted. Figure 3a₁,d₁ present the complete cross-sectional view of the Ag–Si interface on the P⁺ emitter of Cell-A and Cell-B respectively. As shown in Figure 3a₁, only a portion of the silicon nitride (SiN_x) layer at the apex of the pyramid were etched, where the thick glass layer after melt-cooling was accumulated. A dash line is used to indicate the edge of the pyramids before etching in Figure 3a₁. Beneath the etched region, a bowl-shaped area can be observed, which is identified as the current fired contacts (CFC). In contrast, the SiN_x layer was etched away to a great extent by GF-B, leaving only a small area unetched at the base of the pyramid shown in Figure 3d₁. And the glass layer deposited atop the pyramid was exceedingly thin, resulting in a near-direct contact between the Ag and Si. Unlike Cell-A, the CFC structure of Cell-B was notably minute below the apex of the etched pyramid. The Partial enlargement characterized by TEM in high-angle annular dark-field scanning transmission electron microscopy (HAADF-STEM) mode at the CFC structure of Cell-A and Cell-B are shown in Figure 3a₂,d₂ respectively. The dark-field image shown in Figure 3a₂ reveals a significant presence of Ag nanoparticles (NP) in both the glass layer and the CFC region. And an upper dashed line delineates the edge of the original pyramid, while a lower dashed line marks the boundary of the CFC region. Conversely, Ag only deposited in the glass layer with no noticeable Ag deposition observed beneath the etched region as shown in Figure 3d₂ where a dashed line used as a marker for the edge of the pyramid. The mapping distribution of Ag and Si elements in the CFC region of Cell-A are shown in Figure 3a₃,a₄ respectively, and the line distribution of elements (including Si, Ag, and Pb as an indicator of glass layer) are presented in Figure 3b. Combining the results of Figure 3a₃,a₄,b, the Ag NPs were distributed at a depth of ≈ 150 nm beneath the glass layer, which aligns with the dark-field image shown in Figure 3a₂. In contrast,

the mapping distribution for Cell-B are shown in Figure 3d₃,d₄, and the line distribution of elements (including Si, Ag, and Pb along with Te as the indicator of glass layer) are presented in Figure 3e. Based on the results of Figure 3d₃,d₃,e, the distribution positions of Ag and Pb along with Te were nearly identical while a very limited amount of Ag element was diffused into the Si.

Moreover, HRTEM was employed to characterize the detailed information of structure within the CFC regions. The HRTEM images of CFC and the corresponding fast Fourier transformations (FFT) are depicted in Figure 3c₁,c₂ for Cell-A and Figure 3f₁,f₂ for Cell-B, respectively. Figure 3c₁ shows that Ag nanocrystals distributed in the CFC region of Cell-A, while the corresponding FFT in Figure 3c₂ reveals simultaneous lattice diffraction spots for crystalline Si and crystalline Ag. This indicates the formation of Ag–Si eutectic alloy in the P⁺ emitter of Cell-A. It is noteworthy to emphasize that the eutectic temperature of Ag–Si alloy (Si_xAg_y), at ≈ 835 °C,^[15] significantly surpasses the sintering temperature typically employed (lower than 750 °C) in the fabrication of solar cells. And the solid solubility of Ag in Si is very small and Ag usually exists in the form of surface segregation. Therefore, the Ag–Si eutectic reaction occur during the LECO process following the sintering, which required a substantial accumulation of heat in the CFC region for the local temperature to exceed the eutectic point. However, as shown in Figure 3f₁, a large amount of Ag colloids was only distributed in the glass layer while not in the Si emitter. And from the corresponding FFT in Figure 3f₂, the diffraction spots of Ag were observed only coexisted with the diffraction rings of amorphous crystals for glass layer. This suggests that the structure capable to induce localized high temperatures might not completely established at the Cell-B Ag–Si interface after sintering, thereby inhibiting the Ag–Si eutectic reaction.

Hence, the distinct contact structures of Cell-A and Cell-B exerted a significant influence on carrier transport and interface states. The P⁺ emitter of Cell-A contacted the glass layer with densely distributed Ag NPs and the bulk Ag through the Si_xAg_y region. The contact areas were minimal, allowing most of the surface to retain the passivation layer. And the Si_xAg_y effectively reduced the width of the depletion layer, facilitating hole transport via tunneling. This structural improvement can reduce the density of interface states, thereby reducing the carrier capture rate at the interface, reducing the recombination effect, and further enhance the contact quality. Conversely, the P⁺ emitter of Cell-B directly contacted the glass layer and the bulk Ag. Hence, hole transport encountered a significant Schottky barrier, leading to the formation of a high-ohmic contact. And due to a large proportion of the SiN_x passivation layer was etched, the interface states were increased significantly to promote carrier recombination and cause the V_{oc} to drop.

To further delve into the underlying reasons for the differences in LECO activity of Cell-A and Cell-B, the distribution of the glass frits at the interfaces were characterized in various dimensions. The Cell-A and Cell-B before LECO process were treated with nitric acid to corrode the Ag grids but retain the glass layer on the P⁺ emitters, and the top view images are respectively presented in Figure 4a₁,b₁. For easy identification, the glass layers on the Si surface were image-dyed. As shown in Figure 4a₁, the spread of the glass layer (indicated by the blue area) in

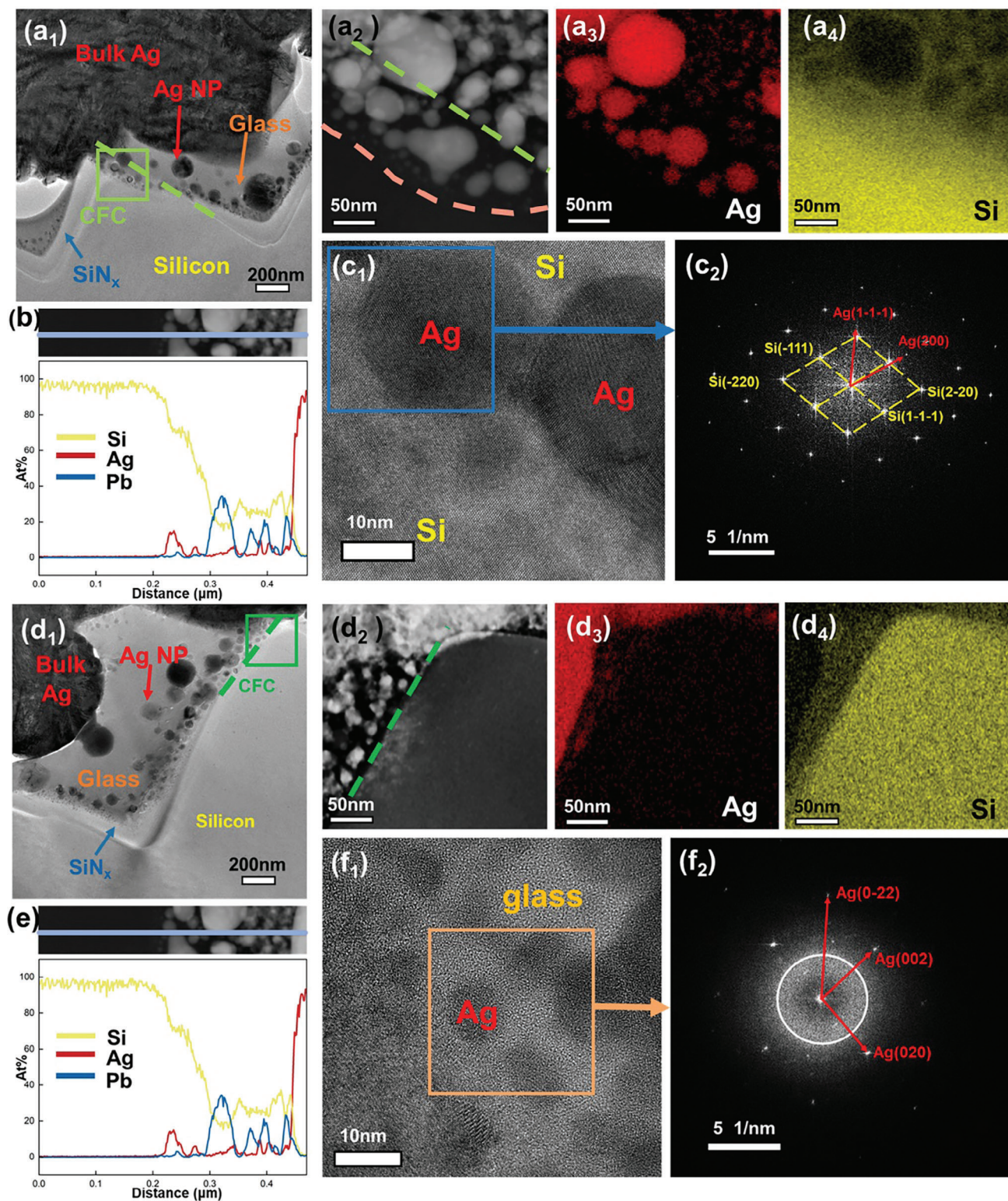


Figure 3. a₁) Cross-section image of Cell-A after LECO treatment by TEM. The box indicates the location of CFC and the dashed line indicates the edges of the pyramids before sintering for Cell-A. a₂) Partial enlargement at the location of CFC by HADDF-STEM. The element distribution spectrum of a₃) Ag and a₄) Si element of CFC for Cell-A. b) The line distribution of elements of CFC for Cell-A. c₁) HRTEM image and the corresponding FFT of CFC for Cell-A. d₁–d₄, e, f₁,f₂) for Cell-B.

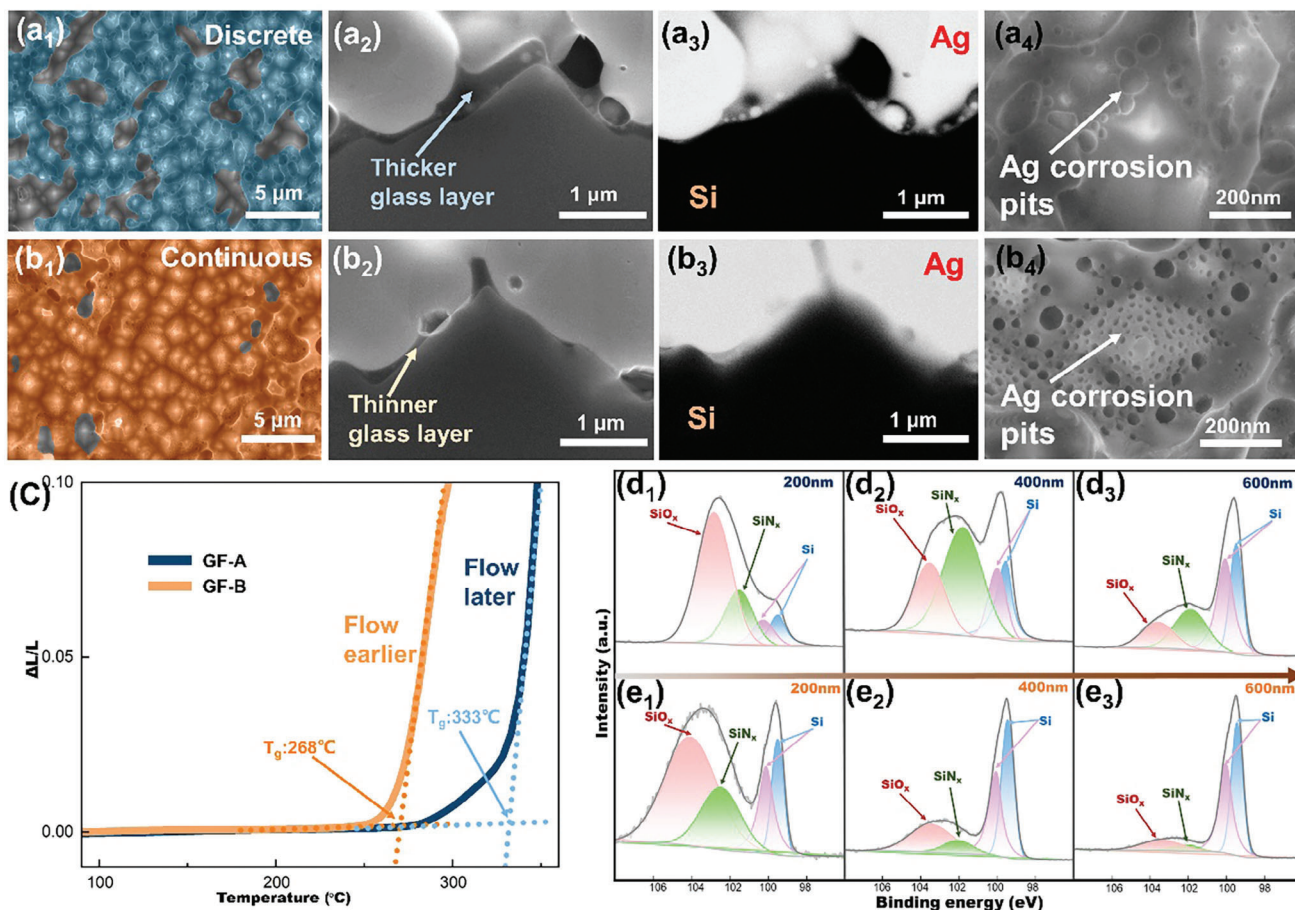


Figure 4. a₁) Top view of Cell-A before LECO treatment with the Ag grid selectively etched. Cross-sectional morphology by SEM in a₂) secondary electron mode and a₃) backscattering mode of Cell-A before LECO treatment. a₄) Partial enlargement of the top view at the Si pyramid of Cell-A. b₁–b₄) for Cell-B. c) TMA curves of the GF-A and GF-B. (d₁–d₃) XPS spectra of Cell-A with the Ag grid selectively corroded before LECO treatment etched by Ar⁺ into 200, 400, and 600 nm respectively, and e₁–e₃) XPS spectra of Cell-B.

Cell-A exhibited a relatively discrete pattern, resulting in the exposure of the bases of many pyramids. While the spread of the glass layer (indicated by the orange area) in Cell-B was relatively continuous and covered almost the entire Si surface. The cross-sectional images of Cell-A before LECO treatment taken in secondary electron mode and backscattering mode are shown in Figure 4a₂,a₃ respectively. As shown in Figure 4a₂,a₃, a thick layer of glass frits was deposited on the apex of the pyramids. Therefore, a nearly thermally insulated structure was established with on the top of the pyramid. Figure 4a₄ displays a partial enlargement at the Si pyramid where larger sized but sparser Ag NPs distributed. And since only the SiN_x on the top was completely etched, a relatively short-circuit current path was constructed top area where a large amount of Joule heat can be accumulated. However, as shown in Figure 4b₁, the glass layer spread more continuously. And the layer of glass frits displayed in Figure 4b₂,b₃ was much thinner and deposited on the pyramids. In hence, the bulk Ag can be almost in direct contact with the top of the pyramid. As shown in Figure 4b₄, smaller-sized but denser Ag corrosion pits were distributed in the glass layer. This interface structure allowed for easier current flow compared to Cell-A resulting in more consistent

resistance across current path everywhere, thereby suppressing the accumulation of local Joule heat.

Moreover, the thermal mechanical analyzer (TMA) was utilized to characterize the thermal properties of GF-A and GF-B. As shown in Figure 4c, the T_g of GF-A was 333 °C, and the T_g of GF-B was 268 °C. This suggests that during the sintering process, GF-A diffused to the Ag–Si interface later than GF-B, thereby leading a greater accumulation in more accumulation of glass layer at the top of the pyramids. This is attributed to the instability of the network structure caused by the addition of TeO₂ as an additive into the glass. From the X-ray photoelectron spectroscopy (XPS) results shown in Figure 4d₁–d₃ and Figure 4e₁–e₃, the SiN_x layer in Cell-A was retained to a greater extent than Cell-B at a depth of 200–600 nm from the glass layer.^[16] Our previous studies also demonstrated that the incorporation of TeO₂ into glass frits significantly enhanced the fluidity and promoted more effective SiN_x etching progress.^[17] Therefore, the thermal properties inherent to the network structure of the glass dictated the capability to establish laser-induced localized high-temperature interfaces on P⁺ emitters during the LECO treatment, which was necessary for the construction of CFC.

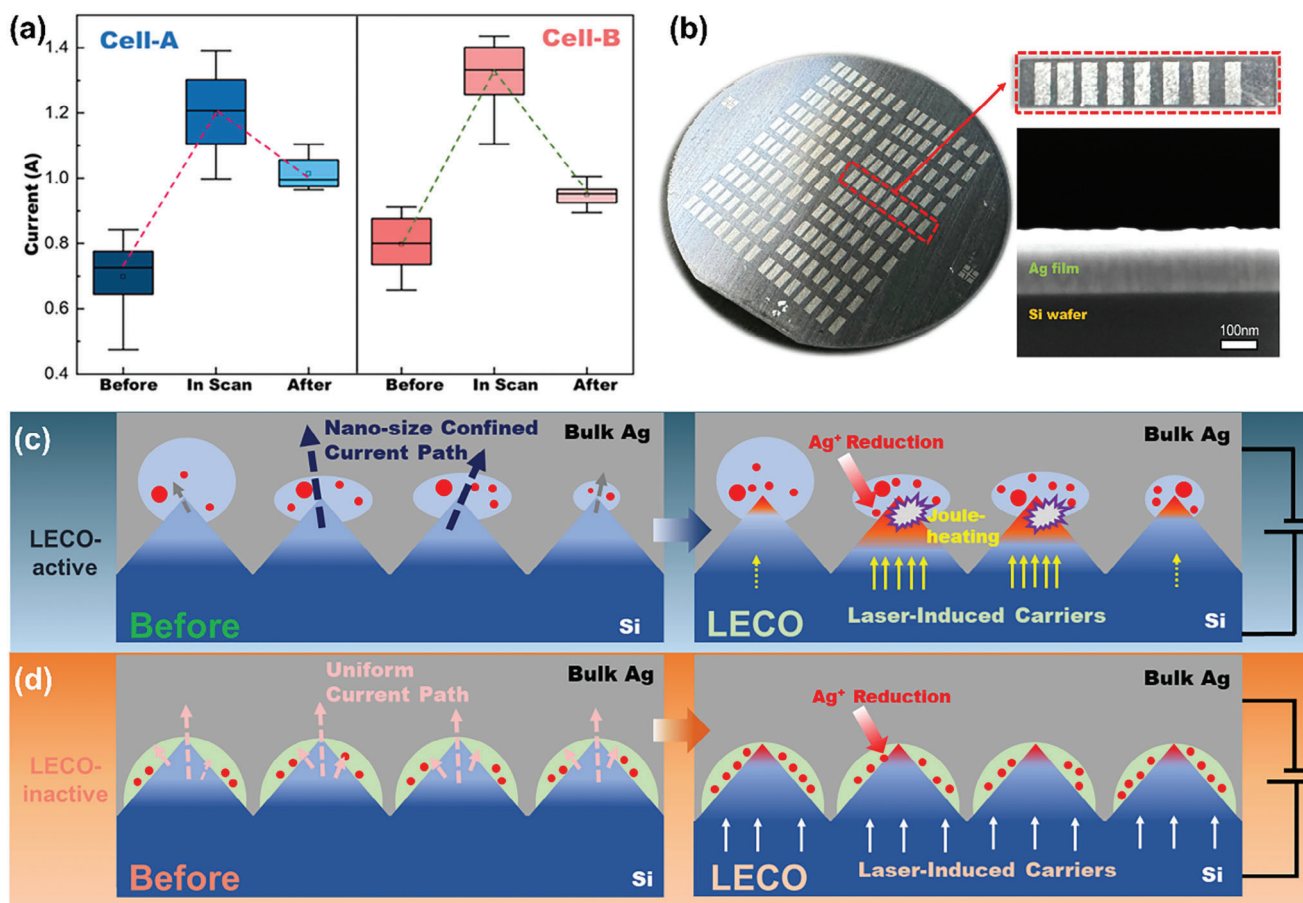


Figure 5. a) Current variations of Cell-A and Cell-B under a 15 V reverse voltage during the LECO treatment. b) Actual picture of a solar cell with evaporated electrodes and a magnified view of the electrode, and a cross-sectional view of the Ag–Si interface under the electrodes after LECO treatment. c) Schematic diagram of the formation mechanism of Ag–Si contacts by LECO treatment on (c) active and d) inactive interface for TOPCon solar Cells.

The current variations recorded with a digital source meter of Cell-A and Cell-B during the LECO treatment are shown in **Figure 5a**, and a constant 15 V reverse voltage was applied to both Cell-A and Cell-B. Prior to laser scanning, Cell-A exhibited an average current value of 0.699 A, whereas Cell-B demonstrated an average current value of 0.797 A. This indicates that there were more short-circuit pathways in Cell-B at the beginning, which was attributed to the greater degree of SiN_x etching. During the laser scanning process, the current values of Cell-A and Cell-B were both enhanced, as 1.19 A and 1.32 A respectively. This suggests that a large number of laser-induced carriers were generated under laser irradiation. Moreover, a larger proportion of the laser-induced carriers were extracted through the Ag–Si interface in Cell-B, while more were consumed by the Joule effect in Cell-A. Following the laser scanning, the current value of Cell-A settled at 1.01 A, and 0.94 A for Cell-B. Compared with the devices before scanning, the currents were both increased, indicating that more low-resistance contacts were established. And the contact quality of Cell-A was significantly superior to that of the other.

Furthermore, we evaporated Ag electrodes on 4-inch P-type Si solar cells to explore the necessary conditions for the formation of LECO activity, and an actual picture of the device was

shown in **Figure 5b**. Before evaporation, the back sides of the solar cells were printed with a commercial n-type Ag paste and subsequently pre-sintered to ensure that ohmic contacts were formed. As shown in **Figure 5b**, the pattern of the evaporated Ag electrodes was designed to comply with the TLM method for comparing the ρ_c before and after the LECO treatment. And from the Cross-section diagram characterized by backscattering mode of the SEM shown in **Figure 5b**, Ag was not diffused into Si and eutectic reaction with Si during the LECO process. The size parameters of the cell with evaporated electrodes and the pattern for evaporated electrodes are shown in **Figure S5** (Supporting Information). Although the Ag layer formed a close contact with Si after being evaporated onto the surface, the contact interface of Ag–Si remains virtually identical across all locations. Therefore, CFC regions were not formed on the surface owing to excellent heat dissipation performance of Ag and the shunting of laser-induced carriers. Furthermore, no dendrites were observed in the Si, as typically seen in the N^+ emitters of the PERC cells after LECO treatment. During a high-temperature process, Ag^+ can be reduced in the N^+ emitters due to a higher density of electrons. And the Ag dendrites formed in N^+ emitter after LECO treatment just fit a typical electric field shape. On the contrary, high-density

of holes were formed in the P emitter under the reverse voltage during LECO process. As a result, the P⁺ emitter lacks sufficient electrons to reduce the Ag⁺. Therefore, utilizing nano-size Joule-heating to initiate a eutectic reaction at localized high temperatures is an optimal approach for achieving the formation of the CFC structure in the P⁺ emitter.

Schematic diagrams illustrating the formation mechanism of Ag–Si contacts on LECO-active and LECO-inactive interfaces for TOPCon solar cells are presented in Figure 5c,d, respectively. In the LECO-active interface, the uneven distribution of the glass layer resulted in only a portion of the pyramid tops forming relatively short-circuited current paths, creating a current-confined interface characterized by a thicker glass layer. During laser scanning, the photocurrent passed to the Ag electrodes through these short-circuit paths under reverse bias. The combination of current confinement and the thermal insulation properties of the glass led to nano-size Joule-heating and promoted the eutectic reaction of Ag–Si. Additionally, Ag⁺ were reduced in the glass layer by externally injected electrons and segregate during cooling process, forming dense conductive particles within the glass layer and effectively enhanced the contact quality. In contrast, the LECO-inactive interface featured a more extensively etched passivation layer, resulting in relatively consistent current path resistances. Moreover, the thinner glass layer in this interface hindered heat accumulation, preventing the induction of localized high temperatures necessary for an effective eutectic reaction between Ag and Si.

3. Conclusion

In summary, we have demonstrated the formation mechanism of CFC through LECO treatment for TOPCon solar cells was a eutectic reaction of Ag–Si by nano-size Joule-heating, indicating that the Ag–Si eutectic alloy structure and the glass layer with high Ag content were the direct reasons for the optimized contact. A LECO-active interface featured both a current-confined structure and a sufficiently thick thermal-insulated glass layer.

The use of GF-A, characterized by a higher T_g and lower flow and spreading ability, resulted in the establishment of a current-confined interface with a thicker glass layer atop the Si pyramids. During LECO treatment, this structure facilitated accumulation of laser-induced Joule heat in nanoscale regions, enabling the eutectic reaction between Ag and Si. In contrast, GF-B, modified with TeO₂ to lower the T_g and improve flow and spreading, led to a more uniformly etched interface with a thinner glass layer, hindering heat accumulation and preventing effective eutectic reaction.

In conclusion, this work not only advances our understanding of metal-silicon contact optimization in solar cells but also introduces novel methodologies for laser-induced synthesis and micro-nano interface engineering. The use of tailored glass frits to achieve current-confined interfaces during LECO treatment offers a promising approach for enhancing the performance of TOPCon solar cells and potentially other photovoltaic technologies. Future research could explore further optimizations in glass frit compositions and process parameters to achieve even higher contact quality and efficiency gains.

Table 1. The element proportions of non-Oxygen components of GF-A and GF-B.

Sample	B [At%]	Si [At%]	Pb [At%]	Al [At%]	Te [At%]
GF-A	35.15	17.10	47.70	0.5	/
GF-B	31.63	15.39	42.93	0.45	10

4. Experimental Section

Materials Synthesis: Preparation of Ag paste: the Ag pastes were formulated by blending 89.0 wt% Ag powder, 2.20 wt% glass frit, 8.80 wt% organic vehicle (consisting of 3% ethyl cellulose, 5% polyamide wax and 92% (2-Butoxyethoxy) ethyl acetate). The mixtures were then thoroughly dispersed using a homogenizer and a three-roll machine. The X-ray polycrystalline diffractometer (XRD) spectrum of Ag powder is shown in Figure S6a (Supporting Information). The element proportions of non-Oxygen components of these two pastes were shown in Table 1.

Preparation of Ag/Al paste: the Ag/Al paste was prepared by mixing 85.85 wt% Ag powder, 2.65 wt% Al powder, 2.21 wt% of GF-A, 9.29 wt% of organic vehicle. The Ag powder and organic vehicle was same as that used in Ag paste.

The rear Ag paste used in this work is made by commercial materials.

Device Fabrication: Fabrication of Cell-A and Cell-B: Ag pastes were applied to Si wafers via a screen-printing process, utilizing a screen with an opening of 26 μm. Subsequently, the Si wafers were sintered in a rapid sintering furnace (Despatch CF-SERIES) to form Ag electrodes. Lastly, the Si wafers underwent LECO treatment, where a laser with a wavelength of 1064 nm was employed at a power of 20 W, while a constant reverse bias voltage of 15 V was applied.

Fabrication of Cell-Ref: The Cell-Ref was prepared using the same process as Cell-A and Cell-B, but with the utilization of Al/Ag paste and without undergoing LECO treatment.

Fabrication of the cell with evaporated electrodes: The Si wafer was cut with a laser from a p-type solar cells, and the P⁺ emitter of the cell was not deposited with SiN_x layer. A series of rectangular electrodes with a length of 2.5 mm and a width of 1 mm were prepared in a linear arrangement on the substrate. The negative photoresist (L300) was applied on the substrate with specific homogenizing parameters, then exposed to UV light under a mask, post-baked, and developed. Ag was evaporated to a thickness of 100nm. Finally, the substrate was ultrasonically cleaned in acetone to remove the photoresist and metal.

Materials Characterizations: The morphology and elemental distribution of the materials and devices were examined by SEM (ZEISS SUPRA-55) with an energy dispersive spectroscopy (EDS, OXFORD, X-MaxN TSR) and TEM (JEM-3200FS, 300 keV) with EDS (OXFORD, X-max 80). XPS measurements were conducted using a Thermo Fisher ESCALAB 250X with a monochromatic Al K X-ray source to obtain the valence states of Si element. XRD measurements with a Bruker D8 Discover diffractometer (Cu Kα radiation with λ = 1.5405(6) Å within the 2θ range of 10–80°) was used to analyze the crystalline structure of Ag powder.

Device Performance Measurements: The electrical parameters of the cells were measured under one sun, AM 1.5G irradiation from a solar simulator (Abet Technologies Model 11000A Sun 3000 Solar Simulator). The specific electrical parameters of cells were measured using Keithley Source-Meter 2602A. The topographic and CPD of the Ag–Si interfaces in cells were measured by utilizing AFM (Dimension Icon, Bruker Co., Germany), with a KPFM microscopy by using Pt/Ir-coated conducting tips (SCM-Pit). In KPFM measurement, the CPD is used to calculate the work function of a material using the following formula:^[18]

$$\Phi = \Phi_{ref} + e \cdot CPD \quad (1)$$

where Φ is the work function of the material being measured, Φ_{ref} is the work function of the reference material. And the e is the charge of the electron.

The R_c and ρ_c values of solar cells were determined through TLM testing. And the electrode configuration used in the TLM test is illustrated in Figure S2b (Supporting Information). The corresponding fitted curve is represented by the equations:^[19]

$$Y = A + Bx \quad (2)$$

where x is the distance between adjacent fingers.

The calculations for R_c and ρ_c are based on the following formulas:

$$A = 2R_c \quad (3)$$

$$B = \frac{R_{sh}}{W} \quad (4)$$

$$\rho_c = \frac{A^2 W}{4B} \quad (5)$$

where W represents the length of finger.

Supporting Information

Supporting Information is available from the Wiley Online Library or from the author.

Conflict of Interest

The authors declare no conflict of interest.

Data Availability Statement

The data that support the findings of this study are available from the corresponding author upon reasonable request.

Keywords

Ag–Si contact, laser enhanced contact optimization, nano-size Joule-heating, solar cell, TOPCon

Received: October 17, 2024
Revised: November 24, 2024
Published online: December 8, 2024

[1] a) F. Feldmann, M. Bivour, C. Reichel, H. Steinkemper, M. Herm, S. W. Glunz, *Sol. Energy Mater. Sol. Cells* **2014**, *131*, 46; b) H. Ullah, S. Czapp, S. Szultka, H. Tariq, U. B. Qasim, H. Imran, *Energies* **2023**, *16*, 715; c) J. K. Zhou, X. L. Su, Q. Huang, B. K. Zhang, J. Yang, Y. Zhao, G. F. Hou, *J. Mater. Chem. A* **2022**, *10*, 20147.

- [2] a) M. C. Xing, T. Q. Wang, F. F. Cao, H. J. Du, M. D. Liao, W. Liu, F. Li, C. X. Xiao, W. R. Zhang, Z. H. Yang, Z. Yuheng, J. C. Ye, *Sol. Energy Mater. Sol. Cells* **2024**, *277*, 113108; b) Y. S. Li, R. Zhou, Z. W. Chen, Y. H. Li, X. Cheng, B. Zhang, J. Chen, Y. Lin, F. Pan, *Small Methods* **2024**, *2400707*.
- [3] Z. Guo, J. H. Liu, X. Y. Zhou, Y. H. Sun, H. P. Yu, S. H. Ma, *Sol. Energy Mater. Sol. Cells* **2024**, *276*, 113065.
- [4] a) G. G. Xing, W. Chen, Y. P. Liu, X. L. Du, *Sol. Energy Mater. Sol. Cells* **2024**, *273*, 112968; b) G. G. Xing, W. Chen, Y. P. Liu, X. L. Du, *Sol. Energy Mater. Sol. Cells* **2024**, *270*, 112814.
- [5] a) P. Afzali, M. Yousefpour, E. Borhani, *J. Mater. Res.* **2016**, *31*, 2457; b) P. Afzali, M. Yousefpour, E. Borhani, *Int. J. Eng.* **2018**, *31*, 2092.
- [6] a) R. Mayberry, K. Myers, V. Chandrasekaran, A. Henning, H. Zhao, U. E. Hofmüller, *36th European Photovoltaic Solar Energy Conference and Exhibition*, EPJ Photovoltaics, Mabledon Place, UK **2019**; b) E. Krassowski, S. Großer, M. Turek, H. Höfller, *37th European Photovoltaic Solar Energy Conference and Exhibition*, EPJ Photovoltaics, Mabledon Place, UK **2020**.
- [7] E. Krassowski, S. Grosser, M. Turek, A. Henning, H. Zhao, presented at 9th Workshop on Metallization and Interconnection for Crystalline Silicon Solar Cells (MIW), Electr Network **2020**.
- [8] S. Grosser, E. Krassowski, S. Swatek, H. M. Zhao, C. Hagendorf, *IEEE J. Photovolt.* **2022**, *12*, 26.
- [9] H. Höfller, F. Simon, E. Krassowski, J. Greulich, 12th International Conference on Crystalline Silicon Photovoltaics (SiliconPV), Konstanz, GERMANY **2022**.
- [10] X. Y. Wu, X. T. Wang, W. G. Yang, J. J. Nie, J. Yuan, M. U. Khan, A. Ciesla, C. Sen, Z. C. Qiao, B. Hoex, *Sol. Energy Mater. Sol. Cells* **2024**, *271*, 112846.
- [11] Y. Fan, S. Zou, Y. L. Zeng, L. F. Dai, Z. P. Wang, Z. Lu, H. Sun, X. S. Zhou, B. C. Liao, X. D. Su, *Sol. RRL* **2024**, *8*, 11.
- [12] a) F. Geml, B. Gapp, S. Johnson, P. Sutton, A. Goode, J. Booth, H. Plagwitz, G. Hahn, *EPJ Photovolt* **2023**, *14*, 8; b) A. Ebong, N. Bezawada, K. Batchu, *Jpn. J. Appl. Phys.* **2017**, *56*, 08mb07.
- [13] S. Deng, Y. L. Cai, U. Roemer, F. J. Ma, F. Rougieux, J. L. Huang, Y. H. Cheng, M. A. Green, N. Song, *Sol. Energy Mater. Sol. Cells* **2024**, *267*, 112704.
- [14] Y. J. Chen, M. J. Zhang, S. Yuan, Y. Qiu, X. B. Wang, X. Jiang, Z. Gao, Y. Lin, F. Pan, *Nano Energy* **2017**, *36*, 303.
- [15] a) Seema, P., S. Kashyap, C. Shekhar, *J. Nanopart. Res.* **2024**, *26*, 160; b) R. W. Olesinski, A. B. Gokhale, G. J. Abbaschian, *Bull. Alloy Phase Diagrams* **1989**, *10*, 635.
- [16] M. Zeghouane, G. Lefevre, S. Labau, M. B. Hachemi, F. Bassani, B. Salem, *Mater. Sci. Semicond. Process* **2024**, *184*, 108851.
- [17] R. Zhou, Y. S. Li, W. C. Tan, Y. Lin, F. Pan, *Sol. RRL* **2024**, *8*, 8.
- [18] a) A. Zahmatkeshsaredorahi, D. S. Jakob, X. G. Xu, *J. Phys. Chem. C* **2024**, *128*, 9813; b) O. C. Olawole, D. De, O. F. Olawole, R. Lamba, E. S. Joel, S. O. Oyedepo, A. A. Ajayi, O. A. Adegbite, F. I. Ezema, S. Naghdi, T. D. Olawole, O. O. Obembe, K. O. Oguniran, *Heliyon* **2022**, *8*, e11030.
- [19] a) D. K. Schroder, D. L. Meier, *IEEE Trans. Electron Devices* **1984**, *31*, 637; b) S. Grover, S. Sahu, P. Zhang, K. O. Davis, S. K. Kurinec, *IEEE 33rd International Conference on Microelectronic Test Structures (ICMTS)*, IEEE, New York **2020**; c) Z. Chen, L. Xu, *Acta Energetica Solaris Sinica* **2014**, *35*, 750.